POLYPUBLIE
Polytechnique Montréal

POLYTECHNIQUE MONTRÉAL
UNIVERSITÉ D'INGÉNIERIE

Document en libre accès dans PolyPublie
Open Access document in PolyPublie

Document publié chez l'éditeur officiel
Document issued by the official publisher

Article

Spiderweb-Inspired, Transparent, Impact-Absorbing Composite

Projectile catch

20 mm

Shibo Zou, Daniel Therriault, Frédérick P. Gosselin

frederick.gosselin@polymtl.ca

HIGHLIGHTS

Transparent composite absorbs impact energy with high hysteresis like spiderweb

Fiber fabric is 3D printed with microstructured sacrificial bonds and hidden length

Fiber-matrix refractive index engineering effectively reduces the composite's haze

Sacrificial bonds and hidden lengths enhance the composite's energy dissipation
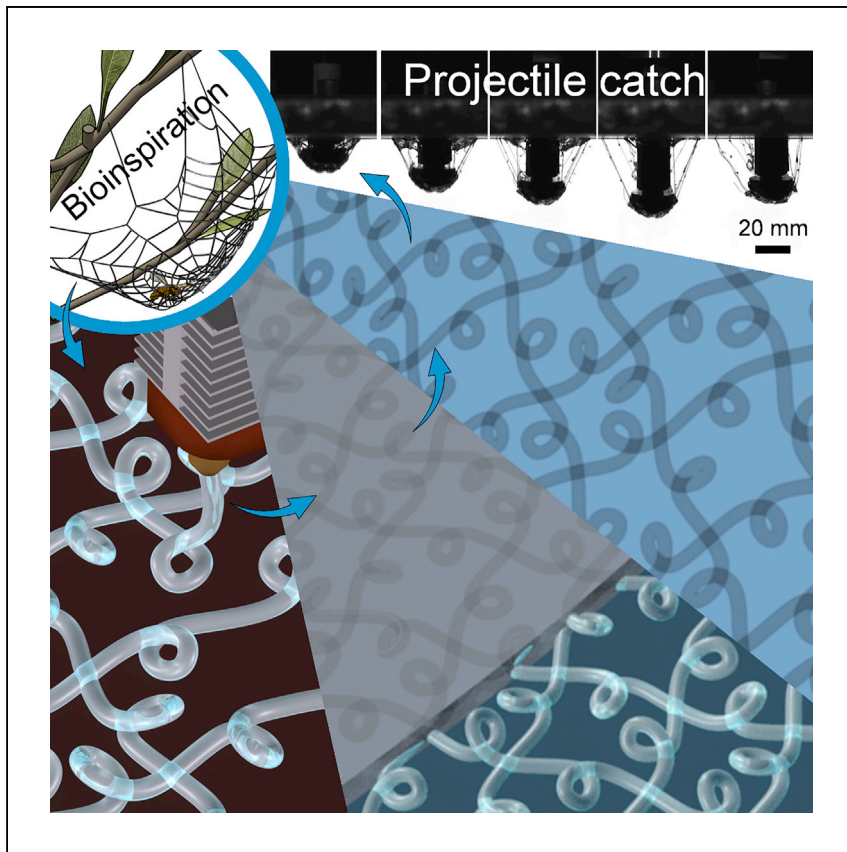
Spiderwebs dissipate a tremendous amount of kinetic energy during prey capture. Zou et al. apply the sacrificial bonds and hidden lengths toughening mechanism found in spider silk to a transparent composite via instability-assisted 3D printing. High optical transmittance and impact energy dissipation are demonstrated.

Article

Spiderweb-Inspired, Transparent, Impact-Absorbing Composite

Shibo Zou,[1] Daniel Therriault,[1] and Frédérick P. Gosselin[1,2,*]

SUMMARY

Transparent materials with high impact absorption are required for many safety-critical engineering systems. Existing transparent tough composites have increased impact resistance but often fail catastrophically because of poor impact absorption. We propose a transparent impact-absorbing composite that reproduces the toughening mechanism involving sacrificial bonds and hidden lengths in spider silk. Our material consists of an elastomer matrix and an instability-assisted, 3D-printed, bidirectional fabric of micro-structured fibers with sacrificial bonds and alternating loops. Under impact, the hidden loops unfold after bond breaking and matrix cracking, resisting impactor penetration with graceful failure. The large-scale plastic deformation of the unfolding loops significantly increases energy dissipation and leads to hysteresis of 95.6% (dissipated energy/total absorbed energy × 100%), minimizing the released elastic energy and reducing the rebounding damage. Our approach opens a new avenue for designing and manufacturing transparent high-energy-absorbing composites for impact protection applications.

INTRODUCTION

Spiderwebs evolved with their weavers to dissipate the tremendous kinetic energy involved during prey capture.[1–3] Unlike other tough biological materials, such as tendons,[4] in which only 10% of the absorbed energy dissipates and 90% is stored as elastic energy in the material,[5] up to 70% of the energy absorbed by the spiderweb dissipates out of the system.[3] The spiderweb dissipates the energy mainly through molecular bond breaking, entropy increase, and internal heat production[3,6,7] in the radial threads.[8] Hence, the elastic energy released upon unloading is minimized to avoid catapulting of insects by the oscillating web after impact. The energy dissipation in the radial threads is attributed to the silk fibril nanostructure, which consists of β sheet nanocrystals and semi-amorphous domains (Figure 1A). [7,9,10] Upon stretching, breaking of hydrogen bonds and uncoiling of protein chains in the semi-amorphous domains contribute to the large extensibility and high energy dissipation. This is known as the sacrificial bonds and hidden lengths (SBHL) mechanism.[11] Variations of this energy-dissipating mechanism have been applied successfully on the molecular scale in hydrogels[12–14] and elastomers,[15–17] resulting in high hysteresis of up to 85%.[14,18] We seek to scale up this molecular-level mechanism on the microscopic scale to make new impact-absorbing architecture composites that can dissipate a large amount of energy and catch the projectile like a spiderweb does (Figure 1B; a general concept overview is available in Video S1).

There are several studies[19–27] that scaled up the SBHL mechanism on the microscopic or macroscopic scale. Sacrificial bonds were constructed via physical fusion

[1]Laboratory for Multiscale Mechanics (LM2), Department of Mechanical Engineering, Research Center for High Performance Polymer and Composite Systems (CREPEC), Polytechnique Montréal, Montréal, QC H3T 1J4, Canada

[2]Lead Contact

*Correspondence: frederick.gosselin@polymtl.ca

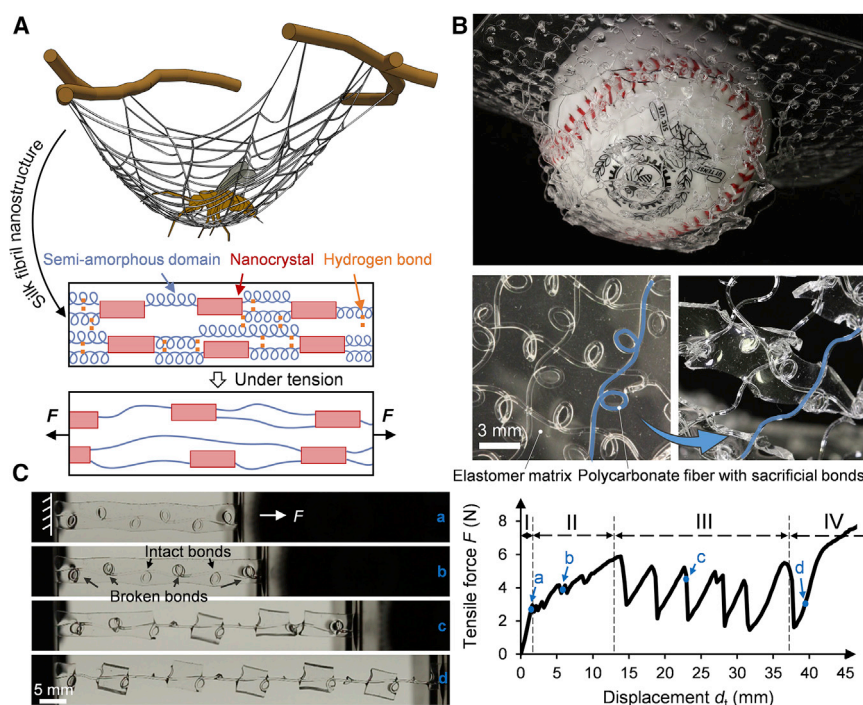https://doi.org/10.1016/j.xcrp.2020.100240

Figure 1. Design of the Spiderweb-Inspired, Transparent, Impact-Absorbing Composite

(A) Schematic of a spiderweb catching flying prey. The high energy dissipation of the spiderweb results from the β sheet nanocrystals and semi-amorphous domains in the silk fibril nanostructure.[7,9,10] The latter contains highly extensible protein chains with intra- and interchain hydrogen bonds. Under tension, breaking of hydrogen bonds within the semi-amorphous domains unravels the hidden portion of the protein chains, increasing the extensibility and toughness of the spider silk.

(B) The spiderweb-inspired, transparent, impact-absorbing composite catching a free-falling baseball after five repeated impacts. The baseball was attached to a 0.5-kg weight and dropped from a 0.66-m height on a falling dart impact tester. Images of the composite before and after impact show breaking of sacrificial bonds and unfolding of hidden lengths, reproducing the energy-dissipating mechanism in spider silk.

(C) Mechanical behavior of a single microstructured fiber-reinforced composite during the tensile test. Camera snapshots of the tensile test at four representative instants (a, b, c, and d) are from the four regimes on the tensile curve, respectively: I, homogeneous stretching of the fiber and matrix; II, breaking of sacrificial bonds in the matrix and fiber-matrix detaching around the loops; III, onset of cracking and segmentation of the matrix around the loops; IV, final stretching of the fiber backbone.

of polymer threads,[19,21,23–25] sliding knots,[20] embedding liquid metals,[26] or 3D-printed hierarchical networks.[22,27] All of these studies observed a similar sequential fracture of sacrificial bonds during which extra energy is dissipated via friction[20] or plasticity.[23] Some studies[19–21,23–25] even physically and functionally resembled the micro-looped silk spun by the recluse spider in nature.[28] However, all of these studies focused on designing a uniaxially toughened system because of the difficulty of integrating the design in a bulk panel without compromising SBHL performance, limiting the material's potential for impact protection applications. Here we propose a transparent and impact-absorbing architecture composite with a bidirectional SBHL system made by instability-assisted fused filament fabrication (IFFF) based on our previous experimental[21] and simulation[23] studies. Under impact, the kinetic energy of the projectile, as demonstrated by a baseball in Figure 1B, is largely dissipated by breaking of sacrificial bonds and unfolding of the hidden loops after matrix cracking. Finally, the composite can catch the projectile gracefully. The mechanical

and optical properties of the fiber and matrix are critical to harness the maximum dissipated energy and achieve excellent transparency: (1) the fiber should have good plasticity to avoid premature failure caused by stress concentrations along the unfolding loop;[23] (2) the matrix should favor sequential unfolding of the hidden loops, which contributes to most of the energy dissipation via plasticity;[23] and (3) the fiber and matrix should have good transparency and, more preferably, a similar refractive index (RI)[29] to reduce geometric scattering[30] at the matrix-fiber interface. Polycarbonate (PC) shows good strain-hardening behavior with a true strain at break of up to 0.8[31] and has ~90% transmittance in the visible light spectrum.[32] It also has a low viscosity below 200 Pa·s when extruded by a fused filament fabrication (FFF) 3D printer at 290°C,[33] making it possible for the viscous coiling regimen[34,35] in IFFF (see details in the Fabric Printing section under Experimental Procedures). Hence, PC is a perfect candidate that fulfills all mechanical, optical, and fabrication requirements. Based on a PC fiber with a refractive index n_{fiber} of 1.58 at 589 nm (Figure S1), two transparent elastomers with different RI values (n_{matrix} = 1.41 or 1.55 at 589 nm; Figure S1) were selected to construct the composites to investigate the RI's effect on the optical properties of the composites. The stiff fiber and soft matrix system has been largely practiced in tough hydrogel[36–38] or viscoelastic polymer[27,39,40] composites. The design principles of these tough composites are to dissipate substantial energy via the fiber and maintain high elasticity via the soft matrix.[41] The resistance to crack propagation is increased considerably compared with the neat matrix, but hysteresis is limited by the high elasticity of the soft matrix. We deliberately chose the elastomer matrix with weak adhesion to PC and low strength to allow the sacrificial bonds to break freely in the matrix (regimen II in Figure 1C) and enable sequential fracture of the matrix and complete unfolding of the hidden loops (regimen III in Figure 1C). Therefore, almost all of the mechanical energy is dissipated out of the system by breaking of sacrificial bonds, friction between the fiber and matrix, matrix cracking, and plastic deformation of the fiber.

RESULTS AND DISCUSSION

Fabric Printing and Mechanical Characterization

Figure 2A shows IFFF fabrication of a two-layer bidirectional fabric of microstructured fibers with SBHL. In the IFFF process, the PC filament is partially melted and then extruded at a speed v_e onto the printing platform from a height h. In the meantime, the extruder is moving at a speed v_m relative to the printing platform. When the speed ratio v_e/v_m exceeds 1, the longitudinal compressive stress in the polymer thread triggers the buckling instability, producing a series of nonlinear patterns.[42,43] Thermally fused sacrificial bonds can be formed by fiber self-intersections in some patterns, such as alternating, coiling, and overlapping patterns.[21] This phenomenon, first called a fluid-mechanical sewing machine (FMSM),[44] has been found not only in viscous threads[44,45] but also in elastic rods.[46] We adapted the quasistatic geometrical model developed by Brun et al.[47] as a fabrication guide to create the bidirectional fabric of microstructured fibers (Note S1; Figure S2). This model has been validated for viscous threads[47,48] and elastic rods,[49] indicating the dominating role of geometry and kinematics over material properties in the FMSM.

To catch the impact projectile at a random location on the composite, the highest possible surface coverage (the fraction of the printing platform area covered by the fiber) of the two-layer fabric of microstructured fibers is desired. Although coiling and overlapping patterns bring the highest surface coverage,[50] the structure of the second-layer coiling loops can be highly distorted because of the disturbed deposition on top of the first-layer loops.[51,52] The distortion will dramatically hinder the
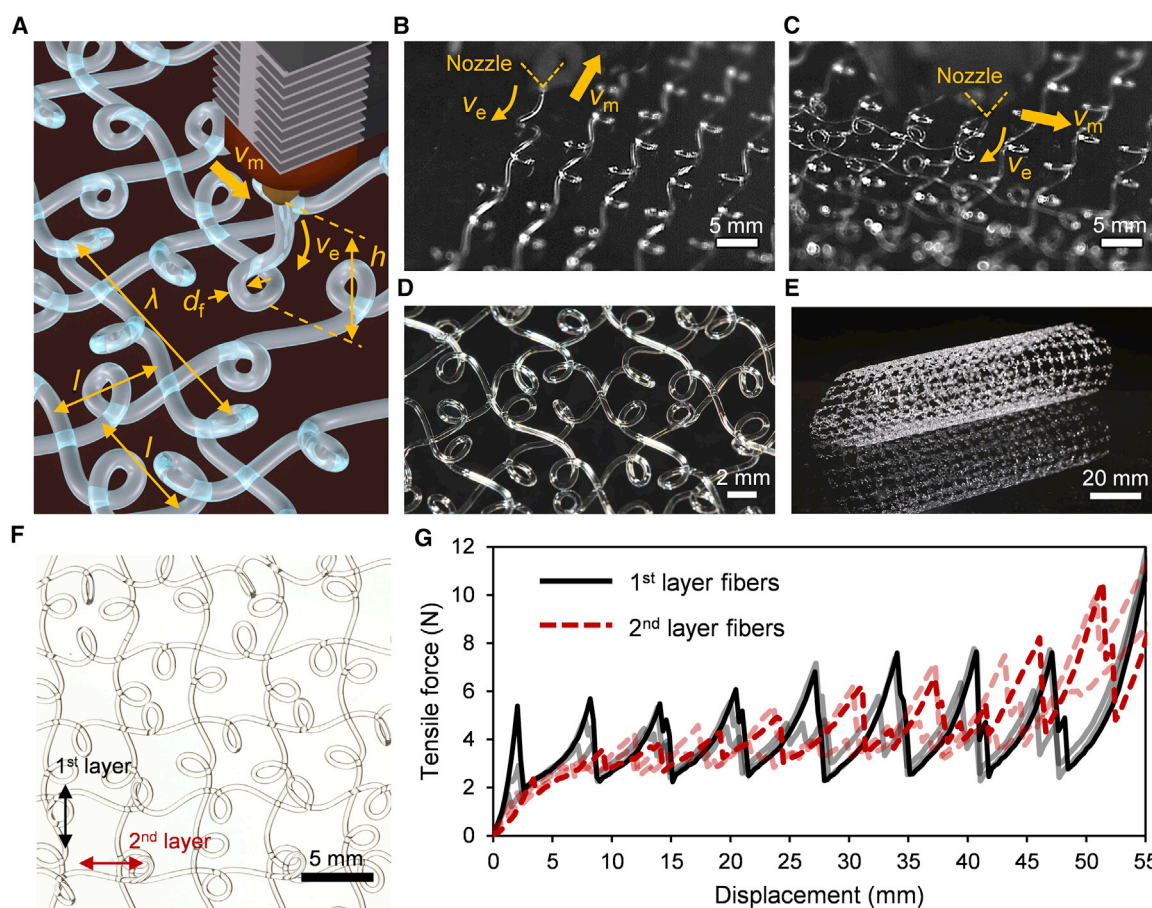
Figure 2. Fabrication and Mechanical Behavior of the Two-Layer Fabric of Microstructured Fibers

(A) Schematic of the IFFF process. The alternating pattern is determined by the ratio of the filament-extruding speed v_e to the extruder-moving speed v_m. The transverse and longitudinal size of the pattern are determined by the ratio of the deposition height h to the fiber diameter d_f. The distance between adjacent deposition paths in both layers is l, which is set to be half of the wavelength of the pattern to reduce loop overlap between the two layers.

(B and C) High-speed camera snapshots of the deposition process of the (B) first and (C) second layer of the fabric of alternating fibers.

(D and E) As-fabricated two-layer fabric (D) at rest and (E) under bending, demonstrating the flexibility and interlayer bonding of the two-layer fabric.

(F) Optical image of the two-layer fabric. The fibers of the first layer are vertical, and the fibers of the second layer are horizontal.

(G) Tensile curves of the first- and second-layer fibers. Three tensile curves are shown for each layer. Besides the two representative curves, other curves are shown in gray and pink for the first- and second-layer fibers, respectively. Each curve represents the tensile test of three fibers in parallel.

energy dissipation of the SBHL system because the distorted fiber tends to fail prematurely.[23] Compared with the coiling and overlapping patterns, the alternating pattern shows a higher potential in avoiding the second-layer loop distortion and achieving a fully functional SBHL system in the bidirectional fabric of microstructured fibers (Figure S2). A surface coverage of ~33% can be achieved by selecting an alternating pattern with a small wavelength. The distance l between each adjacent printing path in both layers is set to be half of the wavelength λ of the alternating pattern. The loops in the first layer can be partially aligned under a stable polymer-extruding speed (Figure 2B). Then the paths of the second layer are designed in the 3D printer g-code to be between the alternating loops of the first layer. This way, the second-layer fiber mostly coils on or between the fiber segments (Figure 2C), not directly on the loops of the first layer. The as-fabricated two-layer fabric of microstructured fibers (Figure 2D) retains sacrificial bonds and alternating loops in both layers. Also,
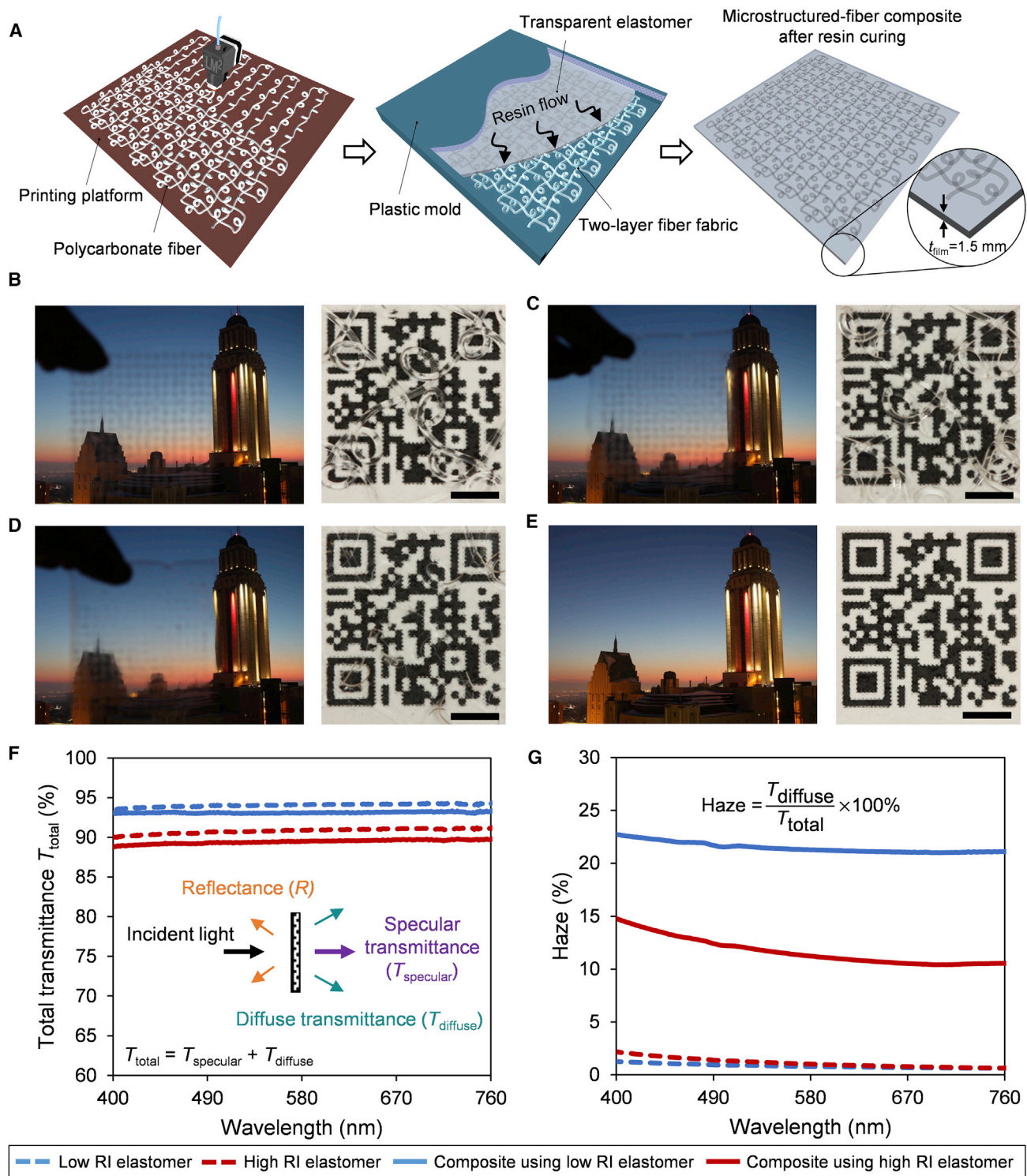
Figure 3. Fabrication and Optical Characterization of the Microstructured Fiber Composite

(A) Schematic of the composite fabrication process. A two-layer fabric consisting of microstructured PC fibers is made by IFFF and then infiltrated by a transparent elastomer in a mold with an inner size of 100 × 100 × 1.5 mm (length × width × thickness). Two transparent elastomers with different RI values (1.41 and 1.55 at 589 nm) were used to make the composite.

(B–D) Comparison of the transparency and image distortion of (B) a two-layer fabric of alternating fibers, (C) a composite film using the low-RI elastomer, and (D) a composite film using the high-RI elastomer in front of a distant building and lying on top of a QR code.

the fabric is flexible and has an interlayer adhesion that is strong enough to keep the fabric integrity under bending (Figure 2E).

To compare the mechanical properties of the fibers from each layer, we manually separated the two layers of a sample of as-fabricated fabric (Figure 2F). For the fibers from each layer, we tested three fibers in parallel in each test and repeated this three times to have a comprehensive comparison of the fibers' tensile properties. The tensile curves of the fibers in both layers are identical (Figure 2G), except the average sacrificial bond strength in the second layer fiber is 79% of that in the first layer, which is probably due to the disturbance by the first-layer fiber during the deposition of the second-layer fiber.

Composite Fabrication and Optical Characterization

Figure 3A shows infiltration of the as-fabricated fabric with an elastomer resin in a plastic mold to obtain a transparent composite after curing. Previous studies of transparent composites with a thickness of a few millimeters used sparse micro-defect arrays (the ratio of defect line spacing to defect width = ~25–100)[53] or matrix-filler RI matching[29,54] to achieve the overall transparency of the composite. In our study, the as-fabricated fabric of alternating fibers has a ratio of fiber spacing to fiber diameter of ~15. A lower ratio than this would cause distortion of the second-layer fiber and hinder energy dissipation of the fabric. A higher ratio than this results in a lower fiber volume fraction, which increases transparency but decreases the energy dissipation capability of the composite. With the selected ratio of ~15, the fabric with functional SBHL in both layers displays decent transparency with a little blur in front of distant objects (Figure 3B). However, the circular cross-section of the fiber causes image distortion, which makes a quick response (QR) code behind the fabric unrecognizable by a QR code scanner (Figure 3B). The image distortion is caused by refraction at the air-fiber interface because of the large relative RI $n^* = n_{fiber}/n_{air} \approx 1.58$. After the fabric is infiltrated with the low-RI elastomer, the n^* at the matrix-fiber interface is reduced to $n_{fiber}/n_{matrix} = 1.58/1.41 = 1.12$. It is ~30% lower than the air-fiber interface, making the QR code scannable (Figure 3C). A further decrease of n^* by the high-RI elastomer ($n^* = n_{fiber}/n_{matrix} = 1.58/1.55 = 1.02$) makes the fiber less visible in the matrix (Figure 3D).

We further characterized the optical transmittance of both elastomers and their composites. The total transmittance (T_{total}) of the low-RI and high-RI elastomer films (Figure 3F, dashed curves) is 94.05% and 90.79% (averaged over the visible light spectrum), respectively. The high-RI elastomer has a lower T_{total}, which is due to a higher n^* ($= n_{elastomer}/n_{air}$) at the air-elastomer interface leading to a higher reflectance R, according to Fresnel's formula at normal incidence:[55]

$$R = \left(\frac{n^* - 1}{n^* + 1}\right)^2. \qquad \text{(Equation 1)}$$

The high-RI elastomer film has 4.65% reflectance ($n^* \approx 1.55$ at 589 nm) per air-elastomer interface, whereas the low-RI elastomer has 2.89% reflectance ($n^* \approx 1.41$ at 589 nm) per interface. The integration of the two-layer fabric of alternating fibers in the elastomer matrix further decreases the T_{total} because of the increase in reflectance at the additional matrix-fiber interfaces (Figure 3F, solid curves). The average T_{total} of the low-RI and high-RI elastomer composite films in the visible light spectrum is 93.12% and 89.45%, respectively.

(E) Reference photos of the distant building and QR code. Both composite films have a thickness $t_{film} = 1.5$ mm. All scale bars represent 3 mm.

(F and G) Total transmittance (F) and haze (G) of the low-RI elastomer film, the high-RI elastomer film, and the composite films based on them. All test films have a thickness $t_{film} = 1.5$ mm.
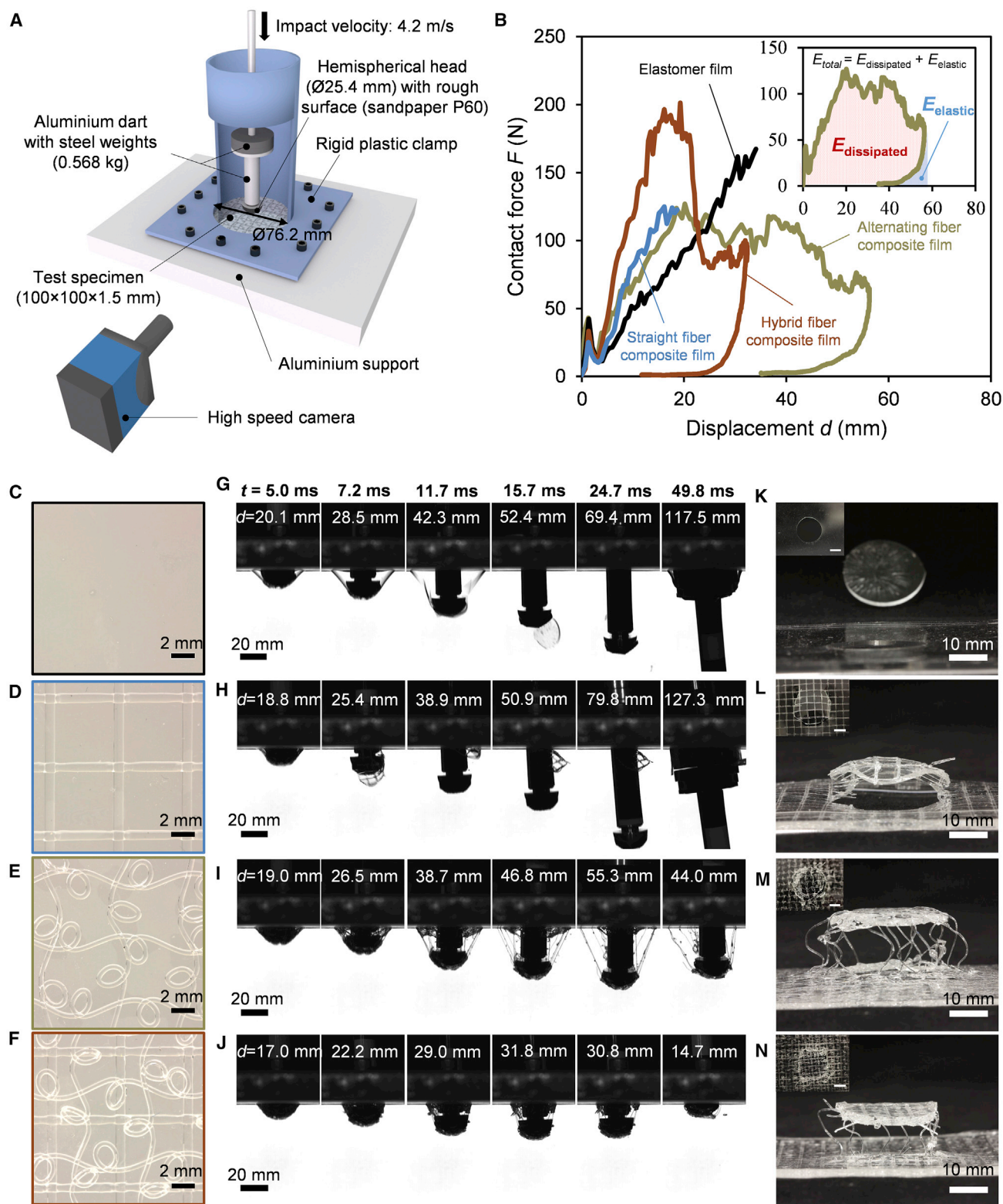
Figure 4. Impact Tests of Different Transparent Films Based on the Low-RI Elastomer

(A) Schematic of the in-house-designed impact test setup. The hemispherical dart head is covered with medium-grit (P60) sandpaper to simulate a realistic projectile with a rough surface.

The transmitted light through the sample film includes a specular component that is perpendicular to the sample surface like incident light and a diffuse component that deviates from the normal direction (Figure 3F, inset). The latter is often related to light scattering in a heterogeneous material.[30] In our case, it is mainly caused by light refraction at the matrix-fiber interface, which is also the main reason for the image distortion. To quantify the matrix RI's influence on light diffusion, we define haze[56] as the ratio of diffuse transmittance to total transmittance. The haze in both elastomer films is very low in the visible light spectrum (Figure 3G, dashed curves), indicating the insignificance of light scattering in both elastomer films. The average haze of the low-RI and high-RI elastomer composite films in the visible light spectrum is 21.48% and 11.66%, respectively. This proves that matrix-fiber RI matching can effectively reduce the light diffusion of the composite.

It should be noted that the difference in the coefficient of thermal expansion between PC ($6.8 \times 10^{-5}/°C$)[32] and the elastomer matrix (low-RI elastomer, ~ 2.6–$3.1 \times 10^{-4}/°C$; high-RI elastomer, $2.1 \times 10^{-4}/°C$; Table S1) would cause debonding at some interfaces between the fiber and the matrix after curing at elevated temperature (Figure S3). Matrix-fiber debonding would reduce optical transmittance and increase the haze of the composite material because of additional interfaces. Because the length scale of matrix-fiber debonding is more than one order of magnitude smaller than that of the fiber and composite film, the influence of matrix-fiber debonding on the optical properties of the composite is believed to be negligible compared with that of the matrix-fiber RI difference.

Impact Test and Failure Analysis

Because the two elastomers have similar mechanical properties (Table S1), we chose the low-RI elastomer for economic reasons to demonstrate the impact absorption of the composite on a falling dart impact tester (Figures 4A and 4B). We tested four materials: elastomer film (Figure 4C), straight-fiber composite film (Figure 4D), alternating-fiber composite film (Figure 4E), and hybrid-fiber composite film (Figure 4F), which contains the straight-fiber fabric and the alternating-fiber fabric.

To simulate a more realistic projectile with an irregular surface, P60-grade sandpaper was attached to the hemispherical head of the falling dart, which led to microscopic defects in the impacted sample. Based on the static puncture test results (Note S2; Figure S4), we chose an impact energy of 5 J at an impact velocity of 4.2 m/s for all test specimens ($100 \times 100 \times 1.5$ mm). We tested three specimens for each type of film and obtained the contact force-time curves (Figures S5A–S5D). Then we calibrated the displacement of the falling dart with a high-speed camera (see details in the Mechanical Characterization section under Experimental Procedures) and obtained the representative contact force-displacement curve for each type of film (Figure 4B).

(B) Contact force-displacement curves of the elastomer film (black), straight-fiber composite film (blue), alternating-fiber composite film (green), and hybrid fiber composite film (red). The inset illustrates the dissipated energy $E_{dissipated}$ (4.7 J) between the loading and unloading curves and the elastic energy $E_{elastic}$ (0.2 J) under the unloading curve of the alternating-fiber composite film. All test films have a thickness of 1.5 mm.

(C–F) Optical images of the (C) elastomer film, (D) straight-fiber composite film, (E) alternating-fiber composite film, and (F) hybrid-fiber composite film.

(G–J) High-speed camera snapshots of the impact tests of the (G) elastomer film, (H) straight-fiber composite film, (I) alternating-fiber composite film, and (J) hybrid-fiber composite film at six different instants after initial contact ($t = 0$ ms). Because the stiffness varies among the four different specimens, the dart appears at different positions among the four specimens at the same instant. The displacement d, which is defined as the vertical displacement of the dart after initial contact, is marked on each snapshot for each specimen. Under the same impact energy (5 J), the impactor penetrates the elastomer film and straight-fiber composite film. The alternating-fiber composite film and the hybrid-fiber composite film catch the impactor by absorbing a large amount of energy. The release of elastic energy springs the dart back up and results in the unloading curves shown in (B).

(K–N) Optical images of the fractured (K) elastomer film, (L) straight-fiber composite film, (M) alternating-fiber composite film, and (N) hybrid-fiber composite film after the impact tests. Scale bars in the insets represent 10 mm.

Under impact, the elastomer film shows an elastic force increase until the crack initiates at the displacement d = 34.1 mm (Figure 4B, black curve). The crack propagates very quickly around the dart head (Figure 4G) because of the low fracture resistance of this elastomer, which has been demonstrated in previous studies.[18,40] The fractured elastomer film shows a smooth fracture surface (Figure S6A). The dart then penetrates through the circular hole punched in the film (Figure 4K; Video S2). The elastomer film slows down the falling dart from 4.2 m/s to 2.6 m/s. Most of the kinetic energy is stored as elastic strain energy in the film. Hence, after penetration, the residual film bounces up and down drastically.

The straight fiber composite film shows a higher effective stiffness (9.1 N/mm) under impact on the contact force-displacement curve (Figure 4B, blue curve) compared with the elastomer film (5.0 N/mm). The dart also penetrates the straight fiber composite film (Figure 4H; Video S3), but circular crack propagation is finally stopped by the fiber (Figure 4L). The crack is deflected by the straight-fiber fabric, resulting in a more irregular crack path than that of the elastomer film. Fiber breakage happens mostly at the grid intersections (Figure S6B), where the fibers are weakened because of the squeezing of two layers at a restricted height by the nozzle during the printing process. The plastic deformation and fracture of the straight fibers as well as fiber pull-outs dissipate a certain amount of energy that would otherwise drive propagation of the crack.

The alternating-fiber composite film shows a similar stiffening behavior (Figure 4B, green curve) as the straight-fiber composite film at the beginning of the impact but a lower effective stiffness (6.0 N/mm) because of breaking of sacrificial bonds during the stiffening process (regimen II in Figure 1C). After propagation of the circular crack around the impactor footprint, the alternating loops are exposed and unfolded to further dissipate the kinetic energy. The falling dart is finally caught by the alternating-fiber composite film (Figure 4I; Video S4). The contact force-displacement curve shows 95.6% hysteresis ($E_{dissipated}/E_{total}$), meaning that 95.6% of the total absorbed energy is dissipated and only 4.4% is released as elastic energy (Figure 4B, inset). The associated fractured specimen (Figure 4M) shows a much larger energy dissipation zone than the elastomer film (Figure 4K). The fracture surface of the alternating-fiber composite film is much rougher than that of the elastomer film because of the crack deflection of the alternating fiber fabric. Many unfolding fibers are observed in the fractured specimen, indicating breaking of sacrificial bonds during the deformation. Matrix segmentation around the fiber loops is also observed (Figure S6C), but it is not as regular as that in the tensile test shown in Figure 1C. Fiber pull-outs are rare because the alternating fibers break outside of the matrix after loop unfolding. Instead, fiber cut-outs are found around the main circular crack (Figure S6C), where the fiber cuts out from the matrix transversely. The fiber cut-outs are believed to be related to the transverse loading condition and are not seen in the tensile test. The complex fracture pattern indicates that the energy is dissipated by breaking of sacrificial bonds, fiber-matrix sliding, matrix cracking and segmentation, fiber cut-outs, plastic deformation, and fracturing of the unfolding fiber.

We also tested a PC film with a weight of ~1.1 times the weight of the alternating-fiber fabric under the same impact energy (Figure S5E). The falling dart penetrates the PC film within 5 ms after initial contact, proving that the high energy dissipation of the alternating-fiber composite is due to the material architecture rather than material components.

A second impact test with the same amount of energy (5 J) on the fractured alternating-fiber composite film leads to total failure of the specimen, with the falling dart penetrating the film (Figure S7A). In another cyclic impact test with an impact energy of 1.4 J, the alternating-fiber composite film is able to catch the falling dart during the first 4 cycles, with the peak contact force reduced less than 40% after the first cycle (Figure S7B). Apparently, cyclic use of the composite at a constant impact location is restricted because when the alternating fibers are exposed and unfolded, they dissipate much less energy through the final fracture. We assume that the composite can retain its high energy absorption for large cycles at random impact locations, which is beyond the capability of our current impact testing machine.

Embedding the straight-fiber fabric and the alternating-fiber fabric in the elastomer further improves the design. The hybrid-fiber composite film shows 93.7% hysteresis with an even higher effective stiffness (13.9 N/mm) and increased maximum contact force. Similar in nature, the cribellate spider produces a silk thread composed of one straight fiber and one coiled fiber to increase energy dissipation during prey capture.[57] The hybrid-fiber composite film catches the falling dart with smaller displacement (Figure 4J; Video S5) than the alternating-fiber composite film because of the extra energy dissipation by the straight fibers. The fractured specimen shows a similar energy dissipation zone (Figure 4N) as that of the alternating-fiber composite film. Unfolding of alternating fibers can be seen in the fractured specimen, as well as breakage and pull-out of straight fibers (Figure S6D), which is similar to the fracture behavior of the alternating-fiber composite film and straight-fiber composite film. However, matrix segmentation and fiber cut-outs, which are found in the alternating-fiber composite film, are rarely observed in the hybrid-fiber composite film, probably because of restriction by the straight-fiber fabric.

To see whether there is a difference in impact absorption performance between the low-RI and high-RI elastomer-based composites, we made an alternating fiber composite film with the high-RI elastomer and used the same impact condition (Video S6). The high-RI elastomer composite film catches the falling dart with a higher effective stiffness (12.8 N/mm; Figure S8A) than the low-RI elastomer composite film (6.0 N/mm; Figure S8A), which is consistent with the fact that the high-RI elastomer has a higher Young's modulus (5.1 MPa; Table S1) than the low-RI elastomer (~1.32–2.97 MPa; Table S1). The high-RI elastomer composite film shows similar fracture behaviors as the low RI elastomer composite film, such as loop unfolding, matrix cracking, and fiber cut-outs. However, the high-RI elastomer composite film shows a larger fiber cut-out length (Figures S8B and S8C), probably because of its lower strength (1.3 MPa; Table S1) compared with the low-RI elastomer (~3.51–7.65 MPa; Table S1). Because the fiber cut-outs expand the energy dissipation zone, the elastomer matrix thickness can be further optimized based on the elastomer property to take advantage of the fiber cut-outs and increase impact energy dissipation.

In conclusion, our architectural transparent composite reproduces spider silk's SBHL toughening mechanism on the microscopic scale. Breaking of sacrificial bonds and unfolding of hidden loops as well as fiber-matrix sliding, fiber cut-outs, matrix cracking, and segmentation contribute to the high hysteresis, impact absorption, damage tolerance, and graceful failure of the composite. The size and pattern of the fabric of microstructured fibers can be further tailored by instability-assisted 3D printing[19,21,24,25] or electrospinning[50,58] to ensure graceful catching of impact projectiles with different sizes and kinetic energies. Nanoscale mechanisms,[41] such as chain fracturing, reversible crosslinking, and transformable domains in

polymer networks, can be introduced to the fiber[24] and matrix[59] to further increase energy dissipation and add self-healing functionalities. The transparent composite can potentially be used in laminated glasses[53] to increase energy dissipation under impact. The combination of high-RI fiber and low RI-matrix in our study also makes it applicable to optical sensing[60,61] of local deformation (Note S3; Figure S9), giving the composite another potential functionality of self-monitoring.[62] The concept of our impact-absorbing composite with an SBHL toughening mechanism can be further extended to various applications, transparent or not, by replacing the material components with other engineering materials, such as polyether ether ketone (PEEK), Kevlar fiber, etc. Finally, our composite represents a way to design structures to fail gracefully rather than catastrophically. Adapting this design to high-performance materials could allow potential applications for bulletproof or spacecraft windows.

EXPERIMENTAL PROCEDURES

Resource Availability

Lead Contact
Further information requests should be directed to the Lead Contact, Frédérick P. Gosselin (frederick.gosselin@polymtl.ca).

Materials Availability
Commercially available PC filaments and Dow silicone elastomer resins were purchased directly from Top3d Filament (Dongguan, China) and Ellsworth Adhesives (Stoney Creek, Canada), respectively. No new unique reagents were generated in this study.

Data and Code Availability
The authors declare that the data generated in this study are available within the article and the Supplemental Information.

Fabric Printing
A vacuum oven dried the clear PC filament (1.75 mm in diameter) overnight at 65°C. A Prusa i3 3D printer printed the filament at 330°C with a high-temperature extruder kit (Dyze Pro, Dyze Design). Simplify3D software sent the custom-written g-code to the printer. Coogan and Kazmer[33] fitted the following Williams-Landel-Ferry model to the in-line rheological test results of PC filaments on an FFF 3D printer:

$$\eta(T) = 5.18 \times 10^9 e^{\left[-\frac{22.2 \times (T-385)}{51.6 + (T-385)}\right]}, \qquad \text{(Equation 2)}$$

where T = 603.15 K in our study. The model predicts the zero-shear viscosity η = 82.65 Pa·s. We first assumed that the polymer thread out of the nozzle kept the as-calculated viscosity during the deposition process. Then we used the following dimensionless height (H) defined by Ribe et al.[35] to make sure that the deposition stays within the viscous steady coiling regime ($H < 0.08$), where gravity and inertia are negligible compared with viscous forces:

$$H = h\left[\frac{g}{(\eta/\rho)^2}\right]^{\frac{1}{3}}, \qquad \text{(Equation 3)}$$

where the gravitational acceleration g = 9.8 m/s^2 and the PC density ρ = 1,200 kg/m^3, so the deposition height h must be smaller than 6.3 mm to stay within the viscous steady coiling regime. We finally chose h = 5 mm (H = 0.0637) for fabrication of the fabric of microstructured fibers. Because the polymer thread solidifies during the deposition process, the viscosity would increase, which makes the effective H even smaller, ensuring deposition in the viscous steady coiling regime. With this

deposition height, we measured the steady coiling radius R_c = 1.8 mm. We used the following geometric model developed by Brun et al.[48] for a molten-glass sewing machine to approximately predict the pattern:

$$r' = cos\phi + \frac{v_m}{v_e} cos\psi \, , \quad \text{(Equation 4)}$$

$$r\psi' = sin\phi - \frac{v_m}{v_e} sin\psi \, , \text{ and} \quad \text{(Equation 5)}$$

$$\phi' + \psi' = \frac{r}{R_c} sin\left(\pi\sqrt{\frac{|\phi|}{\pi}} \frac{\phi}{|\phi|}\right) sin\left(\frac{\pi}{\sqrt{2}}\right)^{-1} , \quad \text{(Equation 6)}$$

where r, ψ, and ϕ are the three geometric parameters that define the trace of the fiber-platform contact point with respect to the nozzle projection on the platform (Figure S10). The relative moving speed v_m = V_F (V_F is the feed rate parameter in the g-code that defines the relative moving speed between the starting point and ending point). Because of the negligible gravitational stretching,[63] the steady coiling speed in the original model[47] was replaced by the extruding speed v_e, which is obtained by the following equation:

$$v_e = \frac{C_1 L_E V_F}{L_D}\left(\frac{D_{filament}}{C_2 d_{nozzle}}\right)^2 , \quad \text{(Equation 7)}$$

where the extruding length L_E of the filament (with the diameter $D_{filament}$ = 1.75 mm) and the moving distance L_D between the starting point and ending point are parameters in the g-code. The volume flow rate correction factor C_1 represents the extruding efficiency and was calibrated at different volume flow rates (Note S4; Table S2; Figure S11). We chose the volume flow rate $Q = L_E V_F \pi D_{filament}^2/4L_D$ = 12.03 mm^3/s for fabrication of microstructured fibers, for which we established a correction factor C_1 = 0.82. The fiber expansion factor C_2 = 1.09 was measured at this volume flow rate for the nozzle diameter d_{nozzle} = 0.4 mm. The geometric model predicts the occurrence of alternating patterns in the speed ratio range 1.57 < v_e/v_m < 2.23. We finally chose v_e/v_m = 2.06 for fabrication of the alternating pattern because of the balance of high surface coverage and fabric printing ease. The as-printed alternating fiber has a measured wavelength λ = 11.8 mm. Thus, the fiber separation l in both layers was set to 5.9 mm. After deposition of the first layer, an offset was carefully calibrated for the second-layer fiber to be deposited mostly between the first-layer loops. The straight-fiber fabric was printed using the same g-code file in which only the deposition height h was set to 0.4 mm. No instability was involved under this deposition height. The weight of the straight-fiber fabric equals that of the alternating-fiber fabric.

Composite Fabrication

We used polydimethylsiloxane (Sylgard 184, Dow) and methylphenylsiloxane (OE-6550, Dow) as the low-RI and high-RI elastomers, respectively. For each elastomer, a vacuum chamber degassed the resin mixture, and then we transferred the mixture to a 20-mL syringe. A micropump (78-8111C, Cole-Parmer) infiltrated the resin from the syringe into the bottom of the plastic mold (Figure S12) via a Teflon tube. No bubbles were generated during the infiltration process. We selected the mold material based on the curing temperature of the elastomer: acrylic mold (glass transition temperature, 105°C) for the low-RI elastomer and PC mold (glass transition temperature, 147°C) for the high-RI elastomer. All molds have the same cavity size of 100 × 100 × 1.5 mm (length × width × height). After infiltration, an oven cured the low-RI elastomer at 65°C for 4 h and the high-RI elastomer at 140°C for 2 h. We can easily peel the material off the plastic mold without a demolding agent.

Optical Characterization

A vertical ellipsometer (RC2, J.A. Woollam) measured the RI spectrum of the PC fiber and both elastomers (Figure S1). To prepare the PC sample, we cut the filament into small pellets. Then a thermal compressing machine molded the pellets into a thin plate. We used the elastomer film made using the abovementioned infiltration and curing process directly on the ellipsometer.

An ultraviolet-visible spectrometer (Lambda 1050, PerkinElmer) with a 150-mm integrating sphere acquired the optical transmittance[56] of the samples within the visible light spectrum (400–760 nm).[64] All test films have a thickness of 1.5 mm. The spectrometer measured the samples in transmittance with a reference beam collected in air. Each sample was tested for total transmittance and diffuse transmittance. For the latter, we used a light trap at the reflectance port on the integrating sphere to exclude the normally transmitted light beam.

A high-speed camera (MotionBLITZ Cube4, Mikrotron) captured printing of the fabric of alternating fibers at a frame rate of 2,790 Hz (Figures 2B and 2C). We used a Canon EOS Rebel T4i camera for photography of the samples in this paper. The sunset pictures in Figure 3 were taken with a standard zoom lens (Canon EF-S 18–135 mm f/3.5–5.6) at 1-s exposure time and f/5.6. The QR code pictures in Figure 3 were taken with a macro lens (Canon EF 100 mm f/2.8) at 1-s exposure time and f/5.6.

Mechanical Characterization

An electromechanical machine (MTS Insight) tested the tensile properties of the single microstructured fiber-reinforced composite and the fibers from each layer of the bidirectional fabric of alternating fibers with a crosshead speed of 500 mm/min. The former had a width of 5 mm, a thickness of 1.5 mm, and a gauge length of 32 mm. The latter had a gauge length of 51 mm, and each fiber consisted of eight alternating loops.

We built a falling dart impact tester based on ASTM D1709.[65] We scaled down the dart head diameter and the inner diameter of the annular clamp to 25.4 mm and 76.2 mm, respectively. A pneumatic clamp (G94, TestResources) dropped the dart into a guiding tube. We selected a drop height of 0.9 m and total drop weight of 0.568 kg to achieve an impact energy of 5 J. We integrated an electroresistive force sensor (A201-445N, Tekscan) into the falling dart (Figure S13) to measure the contact force. We calibrated the force sensor under static loading. The sensor showed a linear response between the conductance and the applied force (Figure S14). During the impact test, a digital multimeter (PCI-4070, National Instruments) and the LabVIEW program measured the conductance of the sensor at a sampling frequency of 6,475 Hz. A high-speed camera (MotionBLITZ Cube4, Mikrotron) captured the dart motion during the impact at a frame rate of 2,230 Hz. We wrote a MATLAB program to read the dart displacement from the high-speed camera snapshots (Figure S15). We manually chose the initial contact frame from these snapshots and correlated the displacement with the contact force. This correlation was evaluated by the discrepancy δ between the impulse J and the momentum change Δp:

$$\delta = \left| \frac{J - \Delta p}{\Delta p} \right| \times 100\%, \qquad \text{(Equation 8)}$$

where the impulse $J = \int_0^t (F + mg)dt$ was calculated with the contact force-time curve from the LabVIEW measurements, and the momentum change $\Delta p = mv_t - mv_0$ was calculated with the velocity measurements from the high-speed camera snapshots. The as-calculated discrepancy was within 20% for all test specimens.

AUTHOR CONTRIBUTIONS

S.Z., D.T., and F.P.G. designed the research. S.Z. carried out all experiments. S.Z., D.T., and F.P.G. analyzed the data and wrote the manuscript.

DECLARATION OF INTERESTS

The authors declare no competing interests.

REFERENCES

1. Denny, M. (1976). The Physical Properties of Spider's Silk and Their Role in the Design of Orb-Webs. J. Exp. Biol. 65, 483–506.

2. Gosline, J.M., Guerette, P.A., Ortlepp, C.S., and Savage, K.N. (1999). The mechanical design of spider silks: from fibroin sequence to mechanical function. J. Exp. Biol. 202, 3295–3303.

3. Kelly, S.P., Sensenig, A., Lorentz, K.A., and Blackledge, T.A. (2011). Damping capacity is evolutionarily conserved in the radial silk of orb-weaving spiders. Zoology (Jena) 114, 233–238.

4. Ker, R. (2007). Mechanics of tendon, from an engineering perspective. Int. J. Fatigue 29, 1001–1009.

5. Bennett, M.B., Ker, R.F., Imery, N.J., and Alexander, R.McN. (1986). Mechanical properties of various mammalian tendons. J. Zool. 209, 537–548.

6. Gosline, J.M., DeMont, M.E., and Denny, M.W. (1986). The structure and properties of spider silk. Endeavour 10, 37–43.

7. Eles, P.T., and Michal, C.A. (2004). Strain Dependent Local Phase Transitions Observed during Controlled Supercontraction Reveal Mechanisms in Spider Silk. Macromolecules 37, 1342–1345.

8. Sensenig, A.T., Lorentz, K.A., Kelly, S.P., and Blackledge, T.A. (2012). Spider orb webs rely on radial threads to absorb prey kinetic energy. J. R. Soc. Interface 9, 1880–1891.

9. van Beek, J.D., Hess, S., Vollrath, F., and Meier, B.H. (2002). The molecular structure of spider dragline silk: folding and orientation of the protein backbone. Proc. Natl. Acad. Sci. USA 99, 10266–10271.

10. Nova, A., Keten, S., Pugno, N.M., Redaelli, A., and Buehler, M.J. (2010). Molecular and nanostructural mechanisms of deformation, strength and toughness of spider silk fibrils. Nano Lett. 10, 2626–2634.

11. Fantner, G.E., Oroudjev, E., Schitter, G., Golde, L.S., Thurner, P., Finch, M.M., Turner, P., Gutsmann, T., Morse, D.E., Hansma, H., and Hansma, P.K. (2006). Sacrificial bonds and hidden length: unraveling molecular mesostructures in tough materials. Biophys. J. 90, 1411–1418.

12. Sun, J.-Y., Zhao, X., Illeperuma, W.R.K., Chaudhuri, O., Oh, K.H., Mooney, D.J., Vlassak, J.J., and Suo, Z. (2012). Highly stretchable and tough hydrogels. Nature 489, 133–136.

13. Sun, T.L., Kurokawa, T., Kuroda, S., Ihsan, A.B., Akasaki, T., Sato, K., Haque, M.A., Nakajima, T., and Gong, J.P. (2013). Physical hydrogels composed of polyampholytes demonstrate high toughness and viscoelasticity. Nat. Mater. 12, 932–937.

14. Luo, F., Sun, T.L., Nakajima, T., Kurokawa, T., Zhao, Y., Sato, K., Ihsan, A.B., Li, X., Guo, H., and Gong, J.P. (2015). Oppositely charged polyelectrolytes form tough, self-healing, and rebuildable hydrogels. Adv. Mater. 27, 2722–2727.

15. Ducrot, E., Chen, Y., Bulters, M., Sijbesma, R.P., and Creton, C. (2014). Toughening elastomers with sacrificial bonds and watching them break. Science 344, 186–189.

16. Wu, J., Cai, L.-H., and Weitz, D.A. (2017). Tough Self-Healing Elastomers by Molecular Enforced Integration of Covalent and Reversible Networks. Adv. Mater. 29, 1702616.

17. Filippidi, E., Cristiani, T.R., Eisenbach, C.D., Waite, J.H., Israelachvili, J.N., Ahn, B.K., and Valentine, M.T. (2017). Toughening elastomers

using mussel-inspired iron-catechol complexes. Science *358*, 502–505.

18. Wang, Z., Xiang, C., Yao, X., Le Floch, P., Mendez, J., and Suo, Z. (2019). Stretchable materials of high toughness and low hysteresis. Proc. Natl. Acad. Sci. USA *116*, 5967–5972.

19. Guo, S.-Z., Gosselin, F., Guerin, N., Lanouette, A.-M., Heuzey, M.-C., and Therriault, D. (2013). Solvent-cast three-dimensional printing of multifunctional microsystems. Small *9*, 4118–4122.

20. Pugno, N.M. (2014). The "Egg of Columbus" for making the world's toughest fibres. PLoS ONE *9*, e93079.

21. Passieux, R., Guthrie, L., Rad, S.H., Lévesque, M., Therriault, D., and Gosselin, F.P. (2015). Instability-Assisted Direct Writing of Microstructured Fibers Featuring Sacrificial Bonds. Adv. Mater. *27*, 3676–3680.

22. Zhu, F., Cheng, L., Wang, Z.J., Hong, W., Wu, Z.L., Yin, J., Qian, J., and Zheng, Q. (2017). 3D-Printed Ultratough Hydrogel Structures with Titin-like Domains. ACS Appl. Mater. Interfaces *9*, 11363–11367.

23. Zou, S., Therriault, D., and Gosselin, F.P. (2018). Failure mechanisms of coiling fibers with sacrificial bonds made by instability-assisted fused deposition modeling. Soft Matter *14*, 9777–9785.

24. Wu, Q., Zou, S., Gosselin, F.P., Therriault, D., and Heuzey, M.-C. (2018). 3D printing of a self-healing nanocomposite for stretchable sensors. J. Mater. Chem. C Mater. Opt. Electron. Devices *6*, 12180–12186.

25. Wei, H., Cauchy, X., Navas, I.O., Abderrafai, Y., Chizari, K., Sundararaj, U., Liu, Y., Leng, J., and Therriault, D. (2019). Direct 3D Printing of Hybrid Nanofiber-Based Nanocomposites for Highly Conductive and Shape Memory Applications. ACS Appl. Mater. Interfaces *11*, 24523–24532.

26. Cooper, C.B., Joshipura, I.D., Parekh, D.P., Norkett, J., Mailen, R., Miller, V.M., Genzer, J., and Dickey, M.D. (2019). Toughening stretchable fibers via serial fracturing of a metallic core. Sci. Adv. *5*, eaat4600.

27. King, D.R., Okumura, T., Takahashi, R., Kurokawa, T., and Gong, J.P. (2019). Macroscale Double Networks: Design Criteria for Optimizing Strength and Toughness. ACS Appl. Mater. Interfaces *11*, 35343–35353.

28. Koebley, S.R., Vollrath, F., and Schniepp, H.C. (2017). Toughness-enhancing metastructure in the recluse spider's looped ribbon silk. Mater. Horiz. *4*, 377–382.

29. Magrini, T., Bouville, F., Lauria, A., Le Ferrand, H., Niebel, T.P., and Studart, A.R. (2019). Transparent and tough bulk composites inspired by nacre. Nat. Commun. *10*, 2794.

30. Petty, G.W. (2006). A first course in atmospheric radiation (Sundog).

31. Kendall, M.J., and Siviour, C.R. (2014). Experimentally simulating high-rate behaviour: rate and temperature effects in polycarbonate and PMMA. Philos. Trans. A Math. Phys. Eng. Sci. *372*, 20130202.

32. Gauthier, M.M. (1995). Optical Testing of Polymers. In Engineered Materials Handbook Desk Edition, M.M. Gauthier, ed. (ASM International), pp. 439–443.

33. Coogan, T.J., and Kazmer, D.O. (2019). In-line rheological monitoring of fused deposition modeling. J. Rheol. (N.Y.N.Y.) *63*, 141–155.

34. Maleki, M., Habibi, M., Golestanian, R., Ribe, N.M., and Bonn, D. (2004). Liquid rope coiling on a solid surface. Phys. Rev. Lett. *93*, 214502.

35. Ribe, N.M., Habibi, M., and Bonn, D. (2012). Liquid Rope Coiling. Annu. Rev. Fluid Mech. *44*, 249–266.

36. Lin, S., Cao, C., Wang, Q., Gonzalez, M., Dolbow, J.E., and Zhao, X. (2014). Design of stiff, tough and stretchy hydrogel composites via nanoscale hybrid crosslinking and macroscale fiber reinforcement. Soft Matter *10*, 7519–7527.

37. King, D.R., Sun, T.L., Huang, Y., Kurokawa, T., Nonoyama, T., Crosby, A.J., and Gong, J.P. (2015). Extremely tough composites from fabric reinforced polyampholyte hydrogels. Mater. Horiz. *2*, 584–591.

38. Huang, Y., King, D.R., Cui, W., Sun, T.L., Guo, H., Kurokawa, T., Brown, H.R., Hui, C.-Y., and Gong, J.P. (2019). Superior fracture resistance of fiber reinforced polyampholyte hydrogels achieved by extraordinarily large energy-dissipative process zones. J. Mater. Chem. A Mater. Energy Sustain. *7*, 13431–13440.

39. Feng, X., Ma, Z., MacArthur, J.V., Giuffre, C.J., Bastawros, A.F., and Hong, W. (2016). A highly stretchable double-network composite. Soft Matter *12*, 8999–9006.

40. Chang, R., Chen, Z., Yu, C., and Song, J. (2019). An Experimental Study on Stretchy and Tough PDMS/Fabric Composites. J. Appl. Mech. *86*, 011012.

41. Zhao, X. (2014). Multi-scale multi-mechanism design of tough hydrogels: building dissipation into stretchy networks. Soft Matter *10*, 672–687.

42. Morris, S.W., Dawes, J.H.P., Ribe, N.M., and Lister, J.R. (2008). Meandering instability of a viscous thread. Phys. Rev. E Stat. Nonlin. Soft Matter Phys. *77*, 066218.

43. Brun, P.-T., Ribe, N.M., and Audoly, B. (2012). A numerical investigation of the fluid mechanical sewing machine. Phys. Fluids *24*, 043102.

44. Chiu-Webster, S., and Lister, J.R. (2006). The fall of a viscous thread onto a moving surface: a 'fluid-mechanical sewing machine.'. J. Fluid Mech. *569*, 89.

45. Klein, J., Stern, M., Franchin, G., Kayser, M., Inamura, C., Dave, S., Weaver, J.C., Houk, P., Colombo, P., Yang, M., et al. (2015). Additive Manufacturing of Optically Transparent Glass. 3D Printing and Additive Manufacturing *2*, 92–105.

46. Jawed, M.K., Da, F., Joo, J., Grinspun, E., and Reis, P.M. (2014). Coiling of elastic rods on rigid substrates. Proc. Natl. Acad. Sci. USA *111*, 14663–14668.

47. Brun, P.-T., Audoly, B., Ribe, N.M., Eaves, T.S., and Lister, J.R. (2015). Liquid ropes: a geometrical model for thin viscous jet instabilities. Phys. Rev. Lett. *114*, 174501.

48. Brun, P.-T., Inamura, C., Lizardo, D., Franchin, G., Stern, M., Houk, P., and Oxman, N. (2017). The molten glass sewing machine. Philos. Trans. A Math. Phys. Eng. Sci. *375*, 20160156.

49. Jawed, M.K., Brun, P.-T., and Reis, P.M. (2015). A Geometric Model for the Coiling of an Elastic Rod Deployed Onto a Moving Substrate. J. Appl. Mech. *82*, 121007.

50. Li, J., Kong, T., Yu, J., Lee, K.H., Tang, Y.H., Kwok, K.-W., Kim, J.T., and Shum, H.C. (2019). Electrocoiling-guided printing of multiscale architectures at single-wavelength resolution. Lab Chip *19*, 1953–1960.

51. Lipton, J.I., and Lipson, H. (2016). 3D Printing Variable Stiffness Foams Using Viscous Thread Instability. Sci. Rep. *6*, 29996.

52. Wang, D., Jing, L., Liu, H., Huang, D., and Sun, J. (2019). Microscale scaffolds with diverse morphology via electrohydrodynamic jetting for *in vitro* cell culture application. Biomed. Phys. Eng. Express *5*, 025011.

53. Yin, Z., Hannard, F., and Barthelat, F. (2019). Impact-resistant nacre-like transparent materials. Science *364*, 1260–1263.

54. Chen, R., Liu, J., Yang, C., Weitz, D.A., He, H., Li, D., Chen, D., Liu, K., and Bai, H. (2019). Transparent Impact-Resistant Composite Films with Bioinspired Hierarchical Structure. ACS Appl. Mater. Interfaces *11*, 23616–23622.

55. Hébert, M., Hersch, R.D., and Emmel, P. (2014). Fundamentals of Optics and Radiometry for Color Reproduction. In Handbook of Digital Imaging, M. Kriss, ed. (John Wiley & Sons), pp. 1–57.

56. ASTM International. ASTM D1003-13. Standard Test Method for Haze and Luminous Transmittance of Transparent Plastics. https://www.astm.org/Standards/D1003.

57. Piorkowski, D., Blackledge, T.A., Liao, C.-P., Joel, A.-C., Weissbach, M., Wu, C.-L., and Tso, I.-M. (2020). Uncoiling springs promote mechanical functionality of spider cribellate silk. J. Exp. Biol. *223*, jeb215269.

58. Choe, Y.E., and Kim, G.H. (2020). A PCL/cellulose coil-shaped scaffold *via* a modified electrohydrodynamic jetting process. Virtual Phys. Prototyp. *15*, 403–416.

59. Wang, D., Xu, J., Chen, J., Hu, P., Wang, Y., Jiang, W., and Fu, J. (2020). Transparent, Mechanically Strong, Extremely Tough, Self-Recoverable, Healable Supramolecular Elastomers Facilely Fabricated via Dynamic Hard Domains Design for Multifunctional Applications. Adv. Funct. Mater. *30*, 1907109.

60. Zhao, H., O'Brien, K., Li, S., and Shepherd, R.F. (2016). Optoelectronically innervated soft prosthetic hand via stretchable optical waveguides. Sci. Robot. *1*, eaai7529.

61. Leber, A., Cholst, B., Sandt, J., Vogel, N., and Kolle, M. (2018). Stretchable Thermoplastic Elastomer Optical Fibers for Sensing of Extreme Deformations. Adv. Funct. Mater. *29*, 1802629.

62. Rifaie-Graham, O., Apebende, E.A., Bast, L.K., and Bruns, N. (2018). Self-Reporting Fiber-

Reinforced Composites That Mimic the Ability of Biological Materials to Sense and Report Damage. Adv. Mater. *30*, e1705483.

63. Yuk, H., and Zhao, X. (2018). A New 3D Printing Strategy by Harnessing Deformation,

Instability, and Fracture of Viscoelastic Inks. Adv. Mater. *30*, 1704028.

64. ASTM International. ASTM E2297-15. Standard Guide for Use of UV-A and Visible Light Sources and Meters used in the Liquid Penetrant and Magnetic Particle

Methods. https://www.astm.org/Standards/E2297.

65. ASTM International. ASTM D1709-16ae1. Standard Test Methods for Impact Resistance of Plastic Film by the Free-Falling Dart Method. https://www.astm.org/Standards/D1709.